

IMPROVED PHOTOMETRY OF SDSS CROWDED FIELD IMAGES: STRUCTURE AND DARK MATTER CONTENT IN THE DWARF SPHEROIDAL GALAXY LEO I

V. SMOLČIĆ

Max-Planck-Institut für Astronomie, Königstuhl 17, Heidelberg, D-69117, Germany

D. ZUCKER

Institute of Astronomy, University of Cambridge, Madingley Road, Cambridge CB3 0HA, UK

E. F. BELL, M. G. COLEMAN, H. W. RIX, E. SCHINNERER

Max-Planck-Institut für Astronomie, Königstuhl 17, Heidelberg, D-69117, Germany

Ž. IVEZIĆ

Department of Astronomy, University of Washington, Box 351580, Seattle, WA 98195-1580, USA

AND

A. KNIAZEV

South African Astronomical Observatory, Observatory Road, Cape Town, South Africa

Version of 16 June 2006

ABSTRACT

We explore how well crowded field point-source photometry can be accomplished with Sloan Digital Sky Survey (SDSS) data. For this purpose, we present a photometric pipeline based on DoPHOT (Schechter et al. 1993), and tuned for analyzing crowded-field images from the SDSS. Using Monte Carlo simulations we show that the completeness of source extraction is above 80% to an i band AB magnitude of $\lesssim 21$ and a stellar surface density of ~ 200 arcmin⁻². Hence, a specialized data pipeline can be efficiently used for fairly crowded fields, such as nearby resolved galaxies in SDSS images, where the standard SDSS photometric package Photo, when applied in normal survey mode, gives poor results.

We apply our pipeline to an area of ~ 3.55 arcmin² around the dwarf spheroidal galaxy (dSph) Leo I. Using the resulting multi-band (g, i) photometry we construct a high signal-to-noise star-count map of Leo I, utilizing an optimized filter in color-magnitude space. This filter reduces the foreground contamination by $\sim 80\%$ and enhances the central stellar surface density contrast of the dwarf by a factor of $\gtrsim 4$, making this study the deepest wide-field study of the Leo I dSph based on accurate CCD photometry. We find that the projected spatial structure of Leo I is ellipsoidal. The best fitting empirical King model to the stellar-surface density profile yields core and tidal radii of $(6.21 \pm 0.95)'$ and $(11.70 \pm 0.87)'$, respectively. This corresponds to (460 ± 75) pc and (860 ± 86) pc assuming a distance to Leo I of 254^{+19}_{-16} kpc. The radial surface-density profile deviates from the King profile towards outer radii, yet we find no evidence for 'S' shaped or irregular tidal debris out to a stellar surface-density of 4×10^{-3} of the central value. From the luminosity function of all possible Leo I stars, which we carefully extrapolated to faintest magnitudes, we determine the total I_c -band luminosity of Leo I to be $(3.0 \pm 0.3) \times 10^6 L_{I_c, \odot}$. We model the mass of the dSph using the spherical and isotropic Jeans equation and infer a central mass density of $0.07 M_{\odot} \text{ pc}^{-3}$ leading to a central mass-to-light ratio of ~ 3 in I_c band solar units. Assuming that the mass in the system follows the distribution of the visible component, we constrain a lower limit on the total mass of the dSph to be $(1.7 \pm 0.2) \times 10^7 M_{\odot}$. On the other hand, if the mass in Leo I is dominated by a dark-matter (DM) halo with constant density, then the mass within the central $12'$ yields $(2 \pm 0.6) \times 10^8 M_{\odot}$. Combining the inferred mass estimates with the total luminosity leads to a mass-to-light ratio of $\gg 6$ in I_c band solar units, and possibly > 75 if the DM halo dominates the mass and extends further out than $12'$. In summary, our results show that Leo I is a symmetric, relaxed and bound system; this supports the idea that Leo I is a dark-matter dominated system.

Subject headings: surveys; galaxies: Local Group, dwarf, halos; cosmology: dark matter; methods: data analysis; techniques: image processing

1. INTRODUCTION

1.1. *The Local Group as seen by the Sloan Digital Sky Survey*

Studies of the Local Group have been recently invigorated by sensitive multi-wavelength large-area surveys, in particular the Sloan Digital Sky Survey (SDSS; York et al. 2000; Stoughton et al. 2002; Abazajian et al.

2003, 2004, 2005; Adelman-McCarthy et al. 2006). To date SDSS has publicly released high-quality near UV to near IR five-band photometry and accurate astrometry (Pier et al. 2003) for ~ 215 million objects selected over $8000 \square^\circ$ (DR5; Adelman-McCarthy et al. 2007). The survey utilizes highly-automated reduction packages. In particular, the pipeline which extracts the multi-band photometry from SDSS images is called Photo (a detailed description of the pipeline is given in Lupton et al. 2002; see also Stoughton et al. 2002).

The SDSS has had a significant impact on Local Group studies. It has led to the discovery of the faintest known dSphs (Willman et al. 2005; Zucker et al. 2006; Belokurov et al. 2006a,b,d) as well as to new insights into already known dSph galaxies (e.g. Draco dSph; Odenkirchen et al. 2001). Analyses of the SDSS photometric dataset have revealed tidal streams surrounding the Milky Way (for example, Odenkirchen et al. 2001; Yanny et al. 2003; Grillmair & Dionatos 2006; Belokurov et al. 2006a,b,d). There have been detailed structural studies of the Galactic halo (Helmi et al. 2003a; Xu et al. 2006) and disk (Helmi et al. 2003b; Juritsch et al. 2005) based on SDSS. However, there is a serious problem associated with the SDSS standard photometric pipeline: Photo does not extract photometry in crowded fields such as globular clusters or nearby galaxies (see §2 for details). For example, the photometry is incomplete for the SDSS fields¹ at the centre of the Leo I dSph galaxy (see Fig. 1).

The aim of this paper is twofold. First, we present a photometric pipeline targeting SDSS images of crowded stellar fields. This pipeline is based on DoPHOT, a software package developed by Schechter et al. (1993), and is designed to be highly automated. Secondly, we apply this pipeline to a $3.55 \square^\circ$ area centered on the Leo I dSph, and study the properties of the dwarf.

1.2. Leo I dwarf spheroidal galaxy

The dwarf spheroidal (dSph) galaxy Leo I was discovered in the Palomar Sky Survey by Harrington & Wilson (1950). Subsequent studies using photographic plates were substantially hampered by the nearby ($\sim 20'$ south of the dSph's center) first magnitude foreground star Regulus (α Leonis). As a result, the first Leo I color-magnitude diagram (CMD) was published only recently (Fox & Pritchet 1987). Nevertheless, Hodge & Wright (1978) had already reported the presence of an intermediate-age stellar population in the galaxy indicated by an unusually large number of anomalous Cepheids. Later studies based on CCD photometry indicated that the intermediate age stars are the dominant population (Reid & Mould 1991; Lee et al. 1993; Demers et al. 1994). Based on Hubble Space Telescope (HST) observations, Caputo et al. (1999) and Gallart et al. (1999a,b) showed that Leo I has an extended star formation history. The oldest stars in Leo I formed approximately 9 – 13 Gyr ago, while the youngest stars are less than 1 Gyr old. It is this latter trait which makes Leo I unusual compared to most other dSphs. An old stellar population with an age $\gtrsim 10$ Gyr has been found just recently in the outer regions of Leo I

¹ An SDSS field is defined as an imaged area in the sky consisting of five (u, g, i, z) frames.

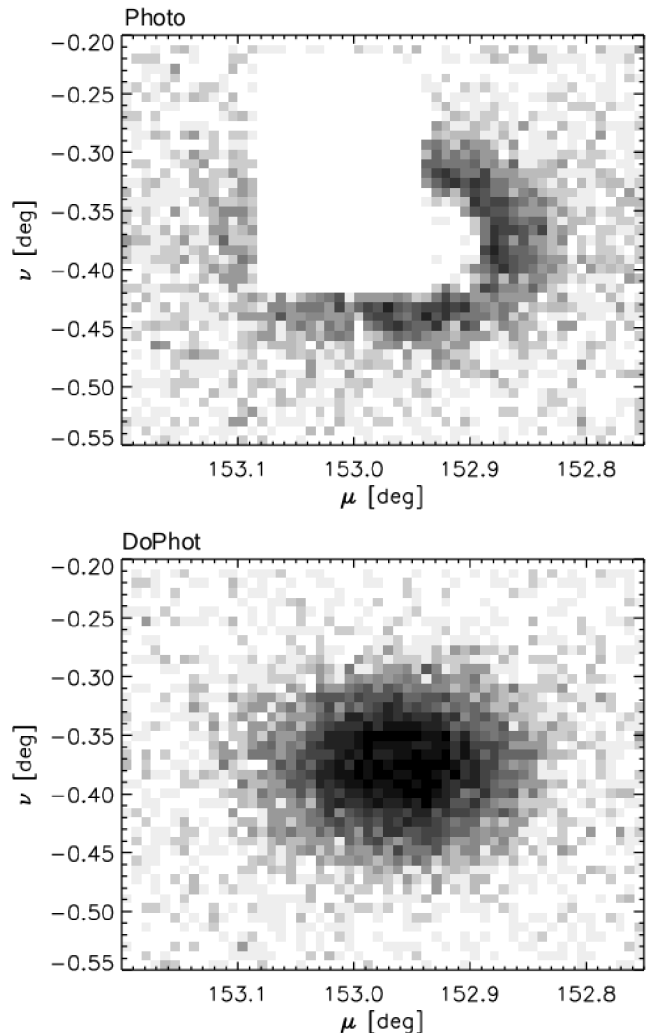


FIG. 1.— Stellar density plots of Leo I shown in Great circle coordinates. The grey-scale is logarithmic, and the same in both panels; darker colors display higher densities. The top panel shows the SDSS (Photo) photometry of Leo I. The bottom panel shows DoPHOT’s photometry for the same area. Both panels show only objects classified as stars by each individual package. Note the missing stars in and around the center of the galaxy in the top (SDSS – Photo) panel.

(Held et al. 2000, 2001).

Leo I is thought to be one of the most distant satellites of the Milky Way in the Local Group. The most recent distance estimate (Bellazzini et al. 2004) puts the galaxy at 254^{+16}_{-19} kpc away from our Galaxy [they infer a distance modulus of $(m - M)_0 = 22.02 \pm 0.13$].

Generally, the high velocity dispersions for Local Group dSphs, combined with dynamical mass estimates, indicate that these systems are dominated by dark matter (DM; for a review see Mateo 1998a). The standard method for estimating mass-to-light (M/L) ratios of pressure-supported systems is to use one-component isotropic King models (King 1962, 1966; Richstone & Tremaine 1986) with simplifying assumptions that the stellar velocity dispersion is isotropic and, critically, that mass follows light. Recent kinematic studies have weakened this latter assumption; velocity dispersion profiles do not demonstrate the characteristic decrease with radius predicted by isotropic King models. Hence it is

likely that ‘traditional’ M/L estimates for dSphs are in fact *lower than the true value*. Specifically, Mateo et al. (1998b) estimate the V band M/L ratio of Leo I to lie in the range of 3.5 – 5.6 (in solar units; see also Mateo 1998a). This result is based on the central velocity dispersion measured for 33 Leo I stars using the structural parameters (such as the core and tidal radii) given in Irwin & Hatzidimitriou (1995; hereafter IH95).

IH95 determined the morphology of eight Local Group dSphs from star counts using digitized *photographic plates*. One major advantage of this study (compared to earlier studies which were largely based on eyeball counts) was that an objective star count method was applied to all dwarfs. However, the usage of photographic plates is for obvious reasons much more restricted than the usage of CCD photometry, which we utilize here. One general problem, which was not taken into account by IH95, is the effect of star blending, which may be significant in regions of high number densities such as the cores of compact stellar systems. Thus, blending may present a serious problem in the determination of structural properties of dSphs as the number densities are not correctly estimated. Here we carefully approach this problem in order to obtain the correct morphological parameters of the Leo I dSph. In summary, better constraints of the structural properties of dSph galaxies are essential for more robust derivations of masses and M/L ratios. In particular, given the large distance from the Milky Way and the great systemic velocity (Mateo et al. 1998b), Leo I plays a crucial role in the estimates of the mass of our Galaxy (e.g. Zaritsky et al. 1989; Zaritsky 1999) and the whole Local Group (Lynden-Bell 1999).

With the advent of multi-wavelength large-area sky surveys, such as the SDSS, the properties of nearby galaxies can be comprehensively investigated (e.g. Odenkirchen et al. 2001). In this paper we focus on deriving structural properties of Leo I utilizing SDSS images. We use these to constrain more robustly the mass and total luminosity of Leo I and finally model the mass of the dSph. We also address the total mass estimates for Leo I with and without the mass-follows-light assumption. Finally, we derive a range of possible M/L ratios of the galaxy utilizing the improved structural parameters.

Our photometric pipeline is described in §2. The extensive tests performed on the pipeline in order to infer the photometric accuracy and completeness are presented in §3. The results on Leo I are given in §§4–6: §4 describes the color-magnitude selection of Leo I candidates, i.e. the construction of a high-contrast map of Leo I, and briefly the color-magnitude diagram (CMD) of the dSph. We constrain the size and structure of Leo I in §5 and derive the total luminosity, mass and M/L ratio in §6. We discuss our results in §7 and summarize them in §8.

2. THE PHOTOMETRIC PIPELINE

The standard SDSS photometric pipeline, Photo, has two main restrictions: (i) it is time limited (to 1 ms/object), and (ii) the number of extracted objects per image cannot exceed a given number. The photometry package therefore does not analyze centers (and sometimes whole frames) of crowded regions (for example, nearby resolved galaxies). This is illustrated in Fig. 1. Here we present a pipeline developed for obtaining high quality photometry from SDSS images of crowded fields.

The pipeline is based on the DoPHOT source extraction package (Schechter et al. 1993) designed to search for objects on a digital image of the sky and to extract positions, magnitudes and classifications for those objects. The package is widely used in the astronomical community and has a proven accuracy (e.g. Reid & Mould 1991; Vogt et al. 1995; Gallart et al. 1999b; Bellazzini et al. 2004). We use a version of DoPHOT 2.0 which was slightly modified by Eugene Magnier.²

In the following work we focus on g , r and i bands since the u and z bands are less sensitive. Our pipeline can be divided into four parts: 1) aligning the SDSS frames and extracting coefficients (from the SDSS tsField³ file) needed for further calculations, 2) adjusting DoPHOT’s input parameters, 3) running DoPHOT on the individual frames and 4) converting the output photometry to the AB magnitude scale and computing several other quantities, as well as extracting the proper astrometry for a given field (see §2.2 for details). We briefly describe the pipeline below.

2.1. DoPHOT’s input parameters

DoPHOT requires an initial list of parameters (fine-tuned for the given image) to run. In order to make the object-extraction from SDSS images fast and highly automated we developed template DoPHOT parameter files for each photometric band. We fine-tuned these parameters and finally adopted the ones giving the best detection rates.

Two sets of parameters required close attention: the ‘aperture box’ values, and those defining the background sky model. Since DoPHOT fits a model point spread function (PSF) to the data (as opposed to a numerically given empirical PSF), it also computes aperture fluxes to correct for the systematic errors introduced by using a model PSF. These ‘aperture box’ parameters were fine-tuned to reproduce the existing SDSS photometry in uncrowded fields, where Photo performs well⁴. The second important parameter set was those defining the background sky model. Crowded fields result in a background sky level which varies significantly across the field, and DoPHOT can model this variation using either a uniform gradient model or a modified Hubble profile (for the latter see e.g. Binney & Tremaine 1987). We adopted the Hubble model since it increased the detection rate by a factor of ~ 3 due to the more realistic background sky description.

These two sets of parameters were then hard-wired into the fine-tuned template input list. Yet, there are two values that need to be specified separately for each frame, namely estimates of seeing and background sky. We created the pipeline in such a way that it measures these two values directly from the image and adds them to the parameter template to create the final input files.

² The entire program is wrapped inside a C program which implements dynamic memory allocation, furthermore the C code interprets command-line arguments and allows compilation under `f2c`.

³ An SDSS tsField file is a binary FITS table which contains parameters relevant for the entire field (for details see www.sdss.org).

⁴ The parameters were tested on fields surrounding the Leo I dSph. Nonetheless, if the need for different aperture corrections (or any of the fixed parameters) arises, the parameters can easily be changed and added to the pipeline without adversely affecting its performance.

2.2. Calibrating DoPHOT's output to the AB and J2000 systems

During its photometry routine, DoPHOT outputs a list of detected objects with several quantities, including the object positions and classification, total and ‘aperture’ magnitudes (with corresponding errors). DoPHOT’s magnitudes are given in the form of $-2.5 \log(\text{DN})$, where DN are counts in units of digital numbers. To convert them to the AB⁵ magnitude scale (for details about the AB photometric system see Fukugita et al. 1996 and references therein) we used the parameters from the SDSS tsField files to calibrate DoPHOT counts:

$$m = -2.5 \log \left(\frac{\text{DN}}{t_{\text{exp}}} \right) - c_0 - c_{\text{ext}} \cdot m_{\text{air}} \quad (1)$$

where t_{exp} is the exposure time ($t_{\text{exp}} = 53.907456$ s), $|c_0|$ is the magnitude that yields DN/t_{exp} of 1 at zero airmass, c_{ext} the extinction coefficient and m_{air} the airmass. The values c_0 , c_{ext} , m_{air} with their uncertainties are extracted from the SDSS tsField file⁶.

A final magnitude correction is calculated via a set of ‘perfect’ stars, those objects which best represent the PSF shape. [To find these stars DoPHOT iterates through the given image starting at the highest level. At a given level, it creates a typical stellar shape using all detected stars within this iteration. Then it fits this shape to a given object and determines the magnitude. This procedure is repeated at each level. If the shape *and* magnitude fits converge for a given object, it is classified as a ‘perfect’ star.] The final correction is then calculated as the median offset between the total and aperture magnitude systems for these perfect stars. The correction is applied to the complete object list, providing a final set of total AB magnitudes (calculated from the total fluxes derived from fitting a model PSF).

The AB magnitude errors are calculated taking into account the errors of the variables used in eq. [1]. Those are then added to the median uncertainty in quadrature to calculate the final uncertainties. Thus, for any given object reported by DoPHOT, the magnitudes are scaled to the AB system, aperture corrected and the uncertainties are reported. This is completed separately for each frame. From the positions in pixel coordinates as given by DoPHOT the J2000 right ascension and declination for each object are recovered. The objects extracted in each frame are then matched between all bands allowing for a maximum separation of $\sim 2.8''$. Thus, a final stellar list with photometric magnitudes and uncertainties in g , r and i is obtained. In order to compare this photometry with the existing SDSS data, the match algorithm is used to find common stars between the two datasets.

3. TESTING DoPHOT

In this section we describe tests performed on SDSS images using our automatic package (see previous section).

⁵ SDSS photometry is intended to be on the AB system (Oke & Gunn 1983; Fukugita et al. 1996), by which a magnitude 0 object should have the same counts as a source of $F_\nu = 3631$ Jy. However, the photometric zeropoints are slightly off the AB standard. Nonetheless, according to the present estimate the (g, r, i) band zeropoints are close to the AB system (~ 0.01 mag). For details see www.sdss.org.

⁶ The SDSS tsField files report $c_0 < 0$.

Our aim was to constrain the photometric accuracy and the detection efficiency of the pipeline, in particular for crowded fields where the SDSS photometric software, Photo, gives poor results (see Fig. 1). The results below demonstrate that our DoPHOT-based pipeline can extract high quality photometry from SDSS crowded-field images.

3.1. Photometry

The accuracy of DoPHOT’s (g, r, i) magnitudes relative to SDSS imaging magnitudes is summarized in Fig. 2 for stars in an un-crowded field. The left column shows the magnitude difference as a function of SDSS magnitude. The middle column shows the histogram of the magnitude difference at the bright end ($\text{mag} < 21$). The distribution of the magnitude difference is symmetric in the r band, while the g and i bands show slight systematic trends caused by the differences between the two pipelines, Photo and DoPHOT. One possible source for this skewed behavior may be the aperture parameters which were used as an input for DoPHOT, and were optimized in the r band. It is also possible that the different sky background estimations used in the two pipelines contribute to these effects. The right column in Fig. 2 displays the magnitude differences normalized by the expected errors determined by adding the SDSS and DoPHOT errors in quadrature. Note, that the errors include both photon noise errors and other systematic uncertainties. The mean equivalent Gaussian width, σ , indicated in each panel, is close to unity and demonstrates that various possible errors in extracting counts do not exceed the noise expected from photon statistics.

3.2. Detection efficiency

In order to estimate the accuracy of DoPHOT’s photometry and the efficiency of recovering stars as a function of both magnitude and stellar density, we performed artificial star tests in crowded and un-crowded fields. The tests were performed separately for (g, r, i) bands. Synthetic stars were generated using the DoPHOT PSF model, which consists of similar ellipses of the form:

$$I(z) = I_0 \left[\sum_{k=0}^3 \frac{1}{k!} z^k \right]^{-1} \quad (2)$$

$$z = \frac{1}{2} (x^2 + y^2) \quad (3)$$

To avoid over-crowding (i.e. blending), the artificial star tests were done via Monte Carlo simulations by adding 100 randomly distributed synthetic stars with an appropriate FWHM into each frame. To assess the photometric accuracy of the recovered stars, the procedure was repeated 100 times. The photometry was then extracted utilizing our pipeline as described in Sec. 2. In Fig. 3 we summarize the photometric accuracy for the same un-crowded field shown in Fig. 2. The results for a crowded field are shown in Fig. 4. The magnitudes are reproduced with the expected accuracy ($\sigma \approx 0.014$), with no systematic errors in the overall magnitude scale (the width of the distribution in the last column is very close to unity). The slight systematic offset in the magnitude differences of $\approx 5 \times 10^{-4}$ and $\approx 5 \times 10^{-3}$ for the un-crowded and crowded field, respectively, is due to the

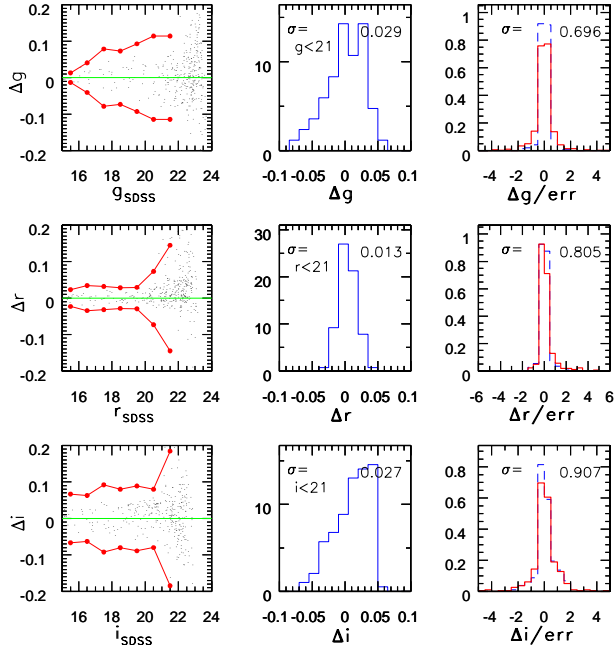


FIG. 2.— The comparison of DoPHOT and SDSS magnitudes in an un-crowded field (run 3631, camcol 3, rerun 40, field 236) in the surrounding of Leo I. The first column displays the magnitude difference as a function of magnitude; the large symbols connected by lines show the $\pm 3\sigma$ envelope. The distribution of magnitude differences at the bright end is displayed in the middle column. The last column shows the distribution of the magnitude differences normalized by the expected errors of DoPHOT’s and Photo’s photometry added in quadrature at the bright end (solid line) and for the full sample (dashed line).

aperture correction (the ‘aperture box’ parameters were set to fit SDSS magnitudes in un-crowded regions). Since the offset is of order of 10^{-3} mag, while the magnitudes are accurate to 10^{-2} mag, the discrepancy is negligible. We conclude that our photometry is sufficiently accurate for robust studies of, for example, nearby galaxies resolved by SDSS.

For a thorough analysis of star counts, luminosity functions, surface density profiles etc., one needs to understand the limits of the source extraction software. It is already well known that detection efficiency declines with stellar brightness. However, since this work is focused on crowded fields, it is essential to understand how the number of retrieved stars depends on the local stellar density. To quantify these dependences we define the *completeness* as the ratio of the number of artificial stars extracted by DoPHOT to the number of artificial stars added to the frame, $n_{\text{output}}/n_{\text{input}}$. Fig. 5 shows the completeness as a function of magnitude for different SDSS fields. We consider a star as *recovered* if i) the position as extracted by DoPHOT matches the position of the inserted artificial star (within a box of $2''$ on a side centered on the star) and ii) the classification for that object given by DoPHOT is a ‘perfect’ star. The uncertainties in Fig. 5 were derived from Poisson errors for the input and output star counts in 1 mag wide bins. Therefore, they reflect the uncertainties due to the low number of artificial stars injected rather than the intrinsic uncertainty of the completeness as a function of magnitude. The fraction of recovered stars falls below 90% at mag-

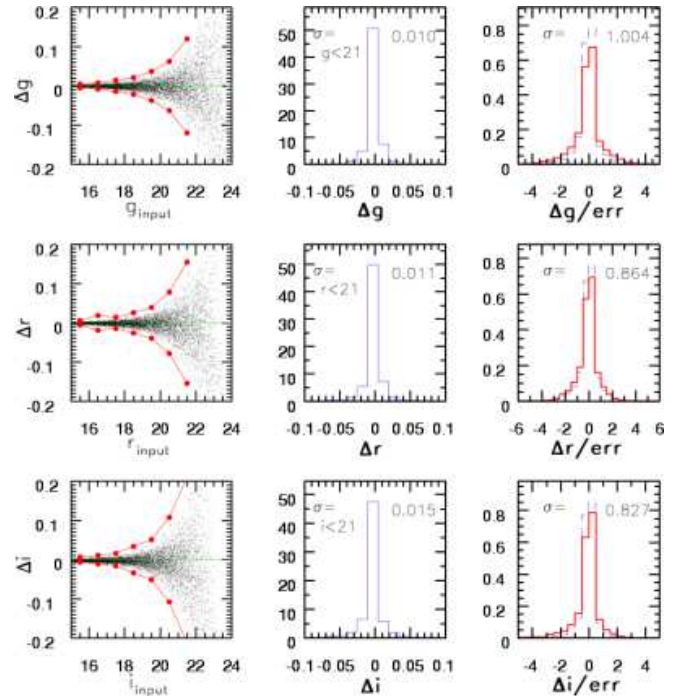


FIG. 3.— Artificial star test results for an un-crowded field (same field as in Fig. 2). The first column displays the magnitude difference of injected and extracted magnitudes as a function of magnitude; the line connected with symbols represents the $\pm 3\sigma$ envelope. The middle column shows the distribution of magnitude differences for $\text{mag} < 21$. The last column displays the distribution of magnitude differences normalized by the expected errors at the bright end (solid line) and for the full sample (dashed line).

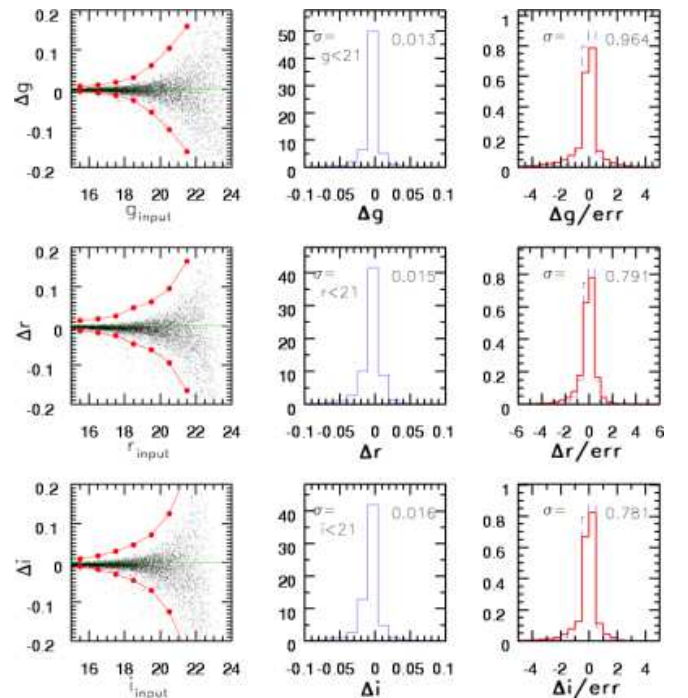


FIG. 4.— Same as Fig. 4, but for a crowded field encompassing a part of Leo I (run 3631, camcol 3, rerun 40, field 238).

nitudes fainter than 20 – 21 (depending on the filter). For reference, the quoted SDSS 95% completeness is in the range of 21.3 – 22.2 mag for the (g, r, i) bands (using

Photo); note, however, that this value is only representative for un-crowded regions.

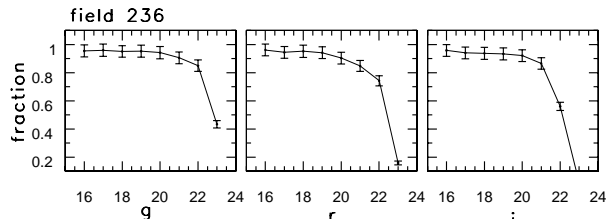


FIG. 5.— The fraction of recovered artificial stars (completeness) as a function of magnitude for an un-crowded field surrounding Leo I (see text for details). Note that the completeness starts declining rapidly for $\text{mag} \gtrsim 21$.

Our next aim was to measure the completeness as a function of stellar density. The following tests were performed on two crowded fields at the center of the Leo I dSph (run 3631, camcol 3, rerun 40, fields 237 and 238). Each field was divided into cells of 50×50 square pixels in area, and the stellar density in each cell was then measured *prior* to artificial star injection. The artificial stars were then placed in the field and recovered using the pipeline, and the completeness fraction was measured for each cell. To ensure we obtained accurate completeness measurements, the Monte Carlo simulations described above were executed for 1000 iterations. Thus, 10^5 stars were randomly placed in each individual (g, r, i) frame. The combined results are displayed in Fig. 6. Note that we show the completeness for four magnitude bins. The crowding at the center of Leo I has no significant effect on stellar recoverability for stars brighter than ~ 20 th magnitude. Stellar crowding reduces the completeness at fainter magnitude bins, inflicting a 10 – 30% loss for stellar densities up to ~ 200 stars/arcmin².

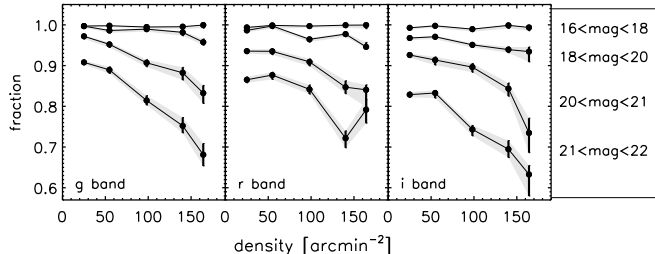


FIG. 6.— The fraction of recovered artificial stars (completeness) as a function of stellar density for different magnitude bins. The panels present the combined artificial star tests ran on fields 237 and 238 (run 3631, camcol 3, rerun 40). The band for which we show the derived completeness is indicated in each panel, and each curve represents the completeness for one magnitude bin, which is indicated in the legend on the right-hand side. Note that the completeness is essentially not a function of stellar density till $\text{mag} \sim 20$.

In Table 1 we summarize the completeness as a function of both magnitude and stellar density for the i band. In latter sections we will use these results to correct star-counts and flux integrals for incompleteness introduced by DoPHOT.

4. PHOTOMETRIC PROPERTIES OF Leo I

In this section we present the construction of a high-contrast map of Leo I utilizing the color-magnitude information, briefly describe the main features of the color-magnitude diagram (CMD) of Leo I, and compare them to previous results.

4.1. Photometric selection of Leo I candidates

Table 2 summarizes the SDSS great circle scans which encompass $\sim 3.55 \square^\circ$ around the Leo I dSph galaxy (see Fig. 7). The photometry extraction was performed as described in §2. An examination of the Schlegel et al. (1998) dust map shows that extinction is not a significant problem for this object; reddening varies by approximately 0.01 mag across the Leo I field. The mean value at the centre of the dSph is $E(B - V) = 0.036$, and thus the entire photometric dataset was corrected using this value. The empty area south of Leo I in Fig. 7 is a result of contamination by the 1st magnitude star Regulus. This and other regions around bright stars are excluded in the further analysis.

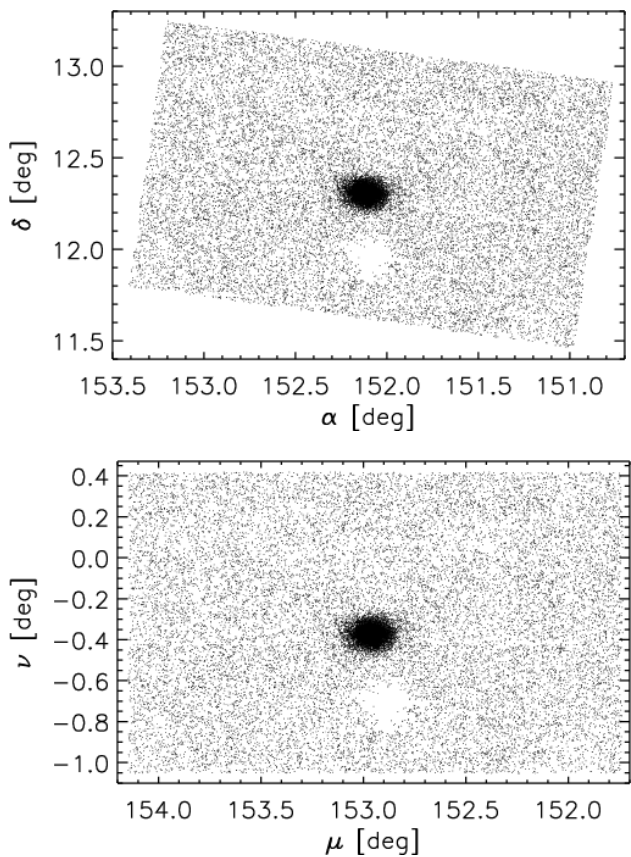


FIG. 7.— Spatial distribution of objects classified as 'perfect' stars by DoPHOT. The shown area covers $\sim 3.55 \square^\circ$ around Leo I. The dSph is visible in the central region of the panel. The top panel shows the distribution in right ascension and declination (J2000), the bottom in great circle coordinates (used for scanning the sky by the SDSS). The empty area in both panels, south of Leo I, is due to contamination by the first magnitude foreground star Regulus (α Leonis).

In order to determine the photometric characteristics of the Leo I population, we selected stars within an ellipse of $6'$ semi-major axis (approximately half the limiting radius) in the central region of Leo I. The distribution of

TABLE 1
i BAND COMPLETENESS AS A FUNCTION OF MAGNITUDE AND STELLAR DENSITY

density [arcmin ⁻²]	fraction [%] <i>i</i> ∈ (16, 18)	upper error	lower error	fraction [%] <i>i</i> ∈ (18, 20)	upper error	lower error	fraction [%] <i>i</i> ∈ (20, 21)	upper error	lower error	fraction [%] <i>i</i> ∈ (21, 22)	upper error	lower error
25.0	99.28	0.02	0.41	96.78	0.19	0.51	92.60	0.37	0.67	82.87	0.63	0.66
54.7	99.77	0.01	0.48	97.08	0.27	0.59	91.38	0.76	1.24	83.27	0.64	1.26
98.1	98.96	0.12	0.62	95.10	0.40	0.64	89.63	0.89	1.26	74.33	0.98	1.59
140.2	99.89	0.02	0.78	93.92	0.66	0.78	84.34	1.39	1.85	69.47	2.13	2.06
164.2	99.37	0.05	00.83	93.44	1.14	2.54	73.47	3.62	4.87	63.27	2.21	5.29

NOTE. — The first column lists the mean density for which the completeness was measured. For the given stellar density range the remaining columns designate the fraction of recovered stars for different *i* band magnitude bins and the upper and lower errors (in %). The uncertainties are Poisson errors of the median completeness for a given magnitude and density bin. The fractions presented here are plotted in Fig. 6.

TABLE 2
 SPECIFICATIONS FOR SDSS IMAGES
 UTILIZED IN THIS PAPER

Run	Rerun	Camcol	Fields
3631	40	2	231-242
3631	40	3	231-242
3631	40	4	231-242
4338	40	1	54-69
4338	40	2	54-69
4338	40	3	54-69
4338	40	4	54-69

NOTE. — Specifications for SDSS images that were used for the scope of this paper. They encompass an area of $\sim 3.55^\circ$ around Leo I. Each field is characterized with a set of four numbers (i.e. run, rerun, camcol, field) which make it unique.

field stars was obtained from stars beyond an ellipse with a semi-major axis of $30'$. The color-magnitude diagram (CMD) for stars in the central region of Leo I is shown in the top left panel in Fig. 8, where the field star distribution is overlaid in contours. As anticipated, the distribution of field stars shows two main populations: the bluer halo stars ($g - r \approx 0.4$) and the redder ($g - r \approx 1.35$) thick disk stars.

To robustly study the dSph galaxy, we needed to construct a map which maximized the number of Leo I stars and minimized the level of field star contamination. In order to do this, we followed the method of Grillmair et al. (1995), which was refined for SDSS photometry by Odenkirchen et al. (2001) in their analysis of the Draco dSph. Stars within the inner region of Leo I form a tight correlation in the $g - r$ vs. $r - i$ plane. This is illustrated in the top right panel in Fig. 7. To quantify the width of this distribution we defined a set of principal axes (c_1, c_2) where c_1 measures the position along the $g - r$ vs. $r - i$ locus, and c_2 the position perpendicular to it:

$$c_1 = 0.920 \cdot (g - r) + 0.391 \cdot (r - i) \quad (4)$$

$$c_2 = -0.391 \cdot (g - r) + 0.920 \cdot (r - i) \quad (5)$$

The bottom panels in Fig. 8 show the CMDs for stars within the inner Leo I region using the principal colors. Since c_2 is essentially a measure of the photometric dispersion, we imposed a cut of $c_2 \leq 2\sigma_{c_2}$ to Leo I stars. Here σ_{c_2} designates the standard deviation of the c_2 distribution measured as a function of *i* magnitude (see bottom right panel in Fig. 8). We imposed an additional magnitude cut of $i < 22$ to the stars in the analyzed area

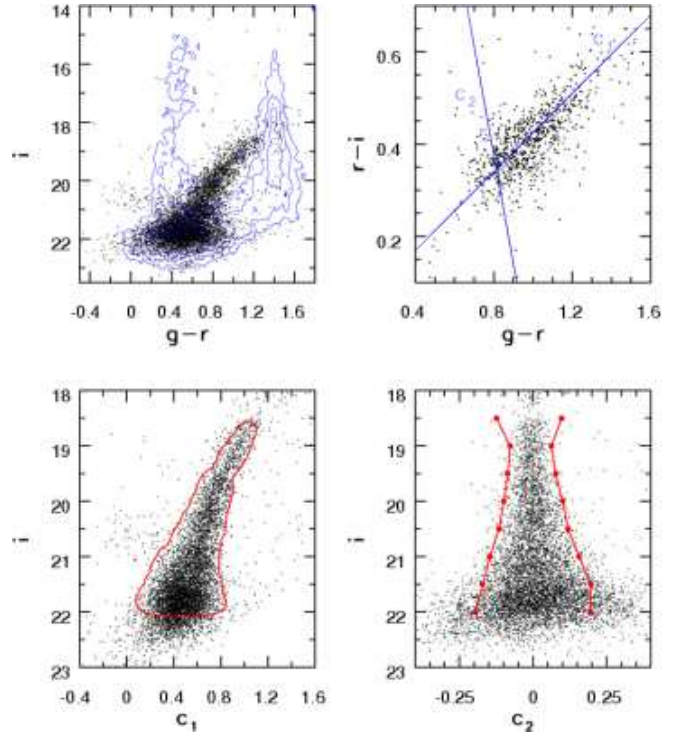


FIG. 8.— Color-magnitude and color-color diagrams of stars in the region around Leo I. In the top left panel dots represent the central region of Leo I, i.e. stars within an ellipse with a semi-major axis of $6'$ in the central region of Leo I. Overlaid contours show the distribution of field stars obtained from stars beyond an ellipse with a semi-major axis of $30'$ centered at Leo I (see text for details). The magnitudes are corrected for reddening. The top right panel shows the $r - i$ vs. $g - r$ diagram for stars with $i > 21$, which were used to obtain the principal component axes (c_1, c_2), which are indicated in the panel (see eqs. [4] & [5] and text for details). Note that the position of the crossing point of the principal axes was shifted for clarity. The bottom panels show the color-magnitude diagrams for the stars in the inner Leo I region (dots) utilizing the principal component colors. The contour in the bottom left panel indicates the optimized photometric filter for the selection of potential Leo I members. The connected large points in the bottom right panel indicate the $\pm 2\sigma$ envelope of the c_2 vs. *i* distribution.

since the completeness decreases significantly at fainter magnitudes and the photometric uncertainties are much higher.

Following the method of Odenkirchen et al. (2001), we constructed CMD functions for the field and Leo I populations. The (c_1, i) CMD was divided into a series of cells, where the cell dimensions were 0.09 mag in color and 0.35 mag in *i*-magnitude. Additionally, each cell was

separated from its ‘neighbors’ by 0.015 mag in color and 0.05 mag in i . This level of overlap between neighboring cells ensured the CMD function was smooth and continuous. As described above, the Leo I stellar population was selected from the inner 6’ of the dwarf, while the field population was taken from the area beyond a radius of 30’. This second value is ~ 2.5 times the Leo I tidal radius, and hence the field area is not expected to contain any of the dSph’s stars. The CMD function was then constructed for both the field and Leo I populations.

As described by Grillmair et al. (1995) and Odenkirchen et al. (2001), we then derived a ‘signal’ for each CMD cell by comparing the Leo I and field populations. For a given cell at position (i, j) , the signal was calculated as:

$$s(i, j) = \frac{n_c(i, j) - gn_f(i, j)}{\sqrt{n_c(i, j) + g^2 n_f(i, j)}}, \quad (6)$$

where $n_c(i, j)$ and $n_f(i, j)$ describe the Leo I (core) and field populations respectively. The factor g is a scaling factor defined as the ratio of the core to field areas. We optimized the population contrast s using a threshold value s_0 such that $s \geq s_0$. The value of s_0 was derived using eq. [2] in Odenkirchen et al. (2001) in such a way that the contrast was optimized for an annulus between 30’ and 60’ from the center of Leo I. The optimal color-magnitude filter mask defined by s_0 is outlined in the bottom left panel in Fig. 8. This filter removed $\sim 80\%$ of the field stars and enhanced the central stellar density contrast by a factor of $\gtrsim 4$.

4.2. Color-magnitude diagram

The morphology of the CMD presented here (see left panels in Fig. 8) agrees very well with those obtained by previous studies (e.g. Reid & Mould 1991; Demers et al. 1994; Gallart et al. 1999a,b; Held et al. 2000, 2001). The most prominent feature is a well defined red giant branch. The red clump is visible in the range $0.1 < g - r < 1$ and $21 < i < 22.5$. The stars in the horizontally extended region at $i \approx 20.5$ and $-0.3 < g - r < 0.3$ correspond to anomalous Cepheids reported first by Wallerstein & Cox (1984) and explored further by e.g. Lee et al. (1993).

5. SIZE AND STRUCTURE OF Leo I

5.1. The center

In this section our aim is to quantify the size and structure of Leo I. Hence it is important to constrain the center of the stellar surface-density distribution of the dSph. In order to do so we spatially binned the color-magnitude filtered Leo I candidate stars and fitted a 2-dimensional Gaussian to this distribution. To account for any artifacts due to our procedure and to robustly estimate the uncertainties, we derived the center, position angle (PA) and ellipticity⁷ of the dwarf using bootstrap-resampling. The mean center in great circle coordinates and the corresponding errors are $\mu = (152.970 \pm 0.003)^\circ$ and $\nu = (-0.365 \pm 0.002)^\circ$. The best fit position angle for great circle coordinates is $PA = (-1.7 \pm 5.7)^\circ$ and the ellipticity is 0.3 ± 0.1 . In the remainder of the paper we will take these coordinates as the center of Leo I and

use the above derived PA and ellipticity values to deduce the surface-density profile of the dSph.

The right ascension and inclination of the ascending node of the great circle scans of the area analyzed here are 95° and 15° , respectively. Hence, the center in J2000 coordinates is at $\alpha = 152.122^\circ \pm 0.003^\circ$ and $\delta = 12.313^\circ \pm 0.003^\circ$, i.e. $10^h 08^m 29.4^s \pm 0.8^s + 12^d 18' 48'' \pm 9''$, the PA is $(-9.2 \pm 5.7)^\circ$ and the ellipticity stays the same. Our PA and ellipticity agree within the uncertainties with the values given in e.g. IH95. The center derived here is roughly consistent with the values from past studies (Zwicky et al. 1961; Gallouët & Heidmann 1971; Dressel & Condon 1976; Falco et al. 1999; see NED for a summary). It is worth noting, however, that the positions of the center of Leo I vary in the literature by $\sim 20'$ and $\sim 30'$ in right ascension and declination, respectively.

5.2. The size

In Fig. 9 we show the projected density profile of the CMD-selected stars. The radial stellar surface-density was obtained by computing stellar densities within elliptical annuli of 1.2’ width starting at the center of Leo I (the center, ellipticity and position angle were chosen as described above). Within each annulus we corrected for incompleteness (see Tab. 1), thereby accounting for the brighter photometric limit of the crowded central region (see also Fig. 6). The datapoints in Fig. 9 display the completeness-corrected density (Σ) above the background (also CMD selected and corrected for incompleteness; $\Sigma_{\text{bkg}} = (0.340 \pm 0.005) \text{ arcmin}^{-2}$) as a function of the radius (i.e. the rms of the outer and inner semi-major axis for a given annulus). The projected background density was estimated using the distribution of field stars beyond an ellipse of semi-major axis of 30’ and the same ellipticity as above centered at Leo I. The error bars indicate quadratically combined Σ and Σ_{bkg} errors, where both take into account completeness and Poisson uncertainties.

To quantify the size of Leo I we fit an empirical King profile (King 1962; hereafter K62) to the stellar surface-density profile. The K62 profile is given as:

$$\Sigma = k \left[\frac{1}{\sqrt{1 + (r/r_c)^2}} - \frac{1}{\sqrt{1 + (r_t/r_c)^2}} \right]^2, \quad (7)$$

$$\Sigma_0 = k \left[1 - \frac{1}{\sqrt{1 + (r_t/r_c)^2}} \right]^2, \quad (8)$$

where Σ is the stellar surface-density, r the radius along the major axis, r_c and r_t are the core and tidal radii, respectively, and Σ_0 is the central surface-density. The best-fit K62 model, shown in Fig. 9, has a reduced χ^2 value of 1.35, and is described with the following parameters: $\Sigma_0 = (137 \pm 54) \text{ arcmin}^{-2}$, $r_c = (6.21 \pm 0.95)'$ and $r_t = (11.70 \pm 0.87)'$. Here the uncertainties correspond to the standard deviation of the fitted parameters based on the non-linear least square fit. The core and tidal radii correspond to $(460 \pm 75) \text{ pc}$ and $(860 \pm 86) \text{ pc}$, respectively, assuming a distance of $254_{-16}^{+19} \text{ kpc}$ (Bellazzini et al. 2004) to Leo I. These parameters are dependent on an accurate measurement of the Leo I center. It is possible that the central coordinates derived in the

⁷ Ellipticity is computed as $1 - b/a$, where a and b are the major and minor semi-axes of the ellipse.

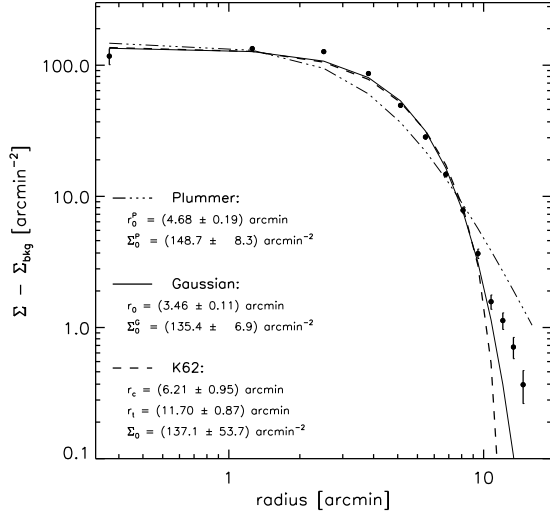


FIG. 9.— Radial profile of the completeness-corrected and background-subtracted stellar density for potential Leo I members (dots). The error bars indicate quadratically combined errors of the background and stellar surface-densities, where both are taken to be dominated by Poisson and completeness uncertainties. Shown are the best-fit King (King 1962; dashed line), Plummer (Plummer 1911; dash-dotted line), and Gaussian (solid line) profiles. We use the latter to estimate the mass of Leo I (see text for details). The best fit parameters for all fitted models are indicated in the panel. Note that the Plummer profile gives the poorest fit to the data.

previous section do not represent the absolute minimum of the gravitational potential of Leo I because the stellar surface-density may not follow a 2-dimensional Gaussian distribution. If we repeat the derivation for determining the center of Leo I described in the previous section, but define the center to be the position where the stellar surface-density has its maximum and fit the K62 model to those data, then the core and tidal radii change by less than 2%.

Our best fit K62 parameters are somewhat different from the results reported in the literature (for an overview see IH95). While the tidal radius is in agreement with previous results (IH95 derive $r_t = (12.6 \pm 1.5)'$ and list previous results in their Table 8), our core radius is substantially higher. r_c is larger by $\sim 50\%$ than the core radius reported in IH95. This is most likely due to the photometry extraction package utilized here, which is specialized for crowded field photometry, as well as the applied robust completeness corrections, which are the largest in the central (i.e. most crowded) regions.

We also find the best fit Plummer law (Plummer 1911), $\Sigma = \Sigma_0^P \left[1 + (r/r_P)^2 \right]^{-2}$, and show it in Fig. 9. The reduced χ^2 of the fit is 3.55, and the central surface density and characteristic scale are $\Sigma_0^P = (149 \pm 8) \text{ arcmin}^{-2}$ and $r_P = (4.7 \pm 0.2)'$. The Plummer model is a less good fit to the data than the K62 profile.

In Fig. 9 we also show the best fit Gaussian profile to the data; $\Sigma = \Sigma_0^G \exp[-r^2/(2r_0^2)]$. The projected stellar density is well presented ($\chi^2 = 0.75$) by a Gaussian out to a radius of $\sim 12'$, with the best fit parameters of $\Sigma_0^G = (135 \pm 7) \text{ arcmin}^{-2}$ and $r_0 = (3.5 \pm 0.1)'$. We utilize this profile in Sec. 6 to model the mass of Leo I.

5.3. Tidal tails?

It is clear from Fig. 9 that the stellar surface density falls off less sharply than the K62 model. Such an excess of stars may indicate tidal extension; on the other hand it may indicate that the (tidally-truncated) K62 model is simply a poor fit to the surface-density profile of a tidally-undisrupted dSph. Some insight into this issue can be gleaned from exploring the 2D density of stars in the outer parts of Leo I.

We display the contour plot of Leo I in Fig. 10. This figure was constructed using the CMD-selected stars, where the background stellar density stated above in §5.2 has been subtracted. Each contour level corresponds to a surface-density point in the radial profile. Thus, the apparent surface-density excesses at large radii seen in Fig. 9 can be directly related to the structures in Fig. 10. For clarity, the contour levels have been divided into two groups: those which are well fit by the K62 model (that is, the points in Fig. 10 at $r \leq 10'$; filled contours) and those which deviate significantly from the model ($r > 10'$; solid and dotted contours). The first four points beyond $r = 10'$ are represented by solid contours, and they describe a roughly elliptical shape. That is, although the radial profile of Leo I appears slightly ‘inflated’ in its outer regions, there is no evidence of a distorted structure (such as the ‘S’-shaped outer structure of the Ursa Minor dSph; Martínez-Delgado et al. 2001; Palma et al. 2003). This argues against any strong tidal disruption of Leo I.

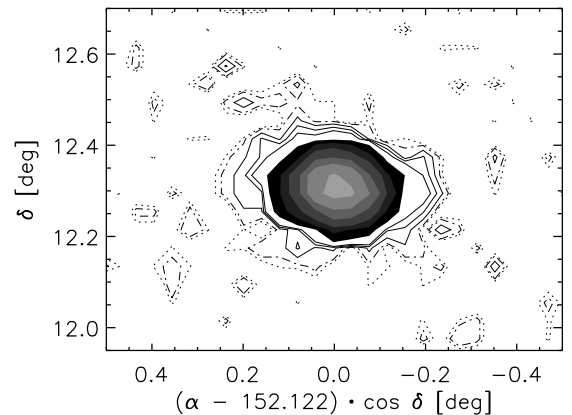


FIG. 10.— The spatial distribution of possible Leo I candidates (see color-magnitude filter in the bottom left panel of Fig. 8) with subtracted field contribution presented in contours. The contour levels correspond to surface densities derived in elliptical annuli of $1.2'$ width (see text for details). The filled contours are equivalent to the surface densities well fit by the K62 profile (first 9 points in Fig. 9). The solid and dotted contours correspond to densities poorly fit by the K62 model (the last 5 points in Fig. 9; see text for details). The lowest density levels (dash-dotted and dotted lines) seem to show asymmetries. The significance of these contours is however below 3σ in the background fluctuation of the field star population.

The two lowest contours (corresponding to the two outermost points in Fig. 9) are displayed with dotted and dashed lines, respectively. A small surface density enhancement is visible to the north-east of Leo I. However, this possible excess of Leo I stars is consistent with less than 3σ in the background fluctuation of the field star population. Hence, within the limit of our data set, there is no clear evidence for a possible tidal disruption of Leo I. This result is not surprising. The relatively large

luminous mass and Galactocentric distance of Leo I argue against its displaying strong signs of tidal disruption. Both Byrd et al. (1994) and Peebles (1995) have modeled the orbit of Leo I and argued that the galaxy had at most one encounter with a large Local Group galaxy in the past. This is consistent with its rather small tidal radius and no evidence for disruption beyond it. Independently, Bowen et al. (1997) showed that there is no evidence for tidally disrupted gas in Leo I based on three QSO/AGN spectra which they utilized to search for absorption by gas within the halo of the dSph.

We proceed in our analysis with the conclusion that Leo I is not tidally disrupted, at least to a magnitude limit of $i = 22$ and a stellar surface-density of 4×10^{-3} of the central surface-density. Large-area coverage with deeper photometry would be needed to resolve whether there are tidal extensions of Leo I at fainter levels.

6. TOTAL LUMINOSITY, MASS AND MASS-TO-LIGHT RATIO OF Leo I

6.1. Total luminosity

The CMD-filtered dataset was used to measure the luminosity function (LF) and total luminosity of Leo I. First, we derived LFs for the field and core regions of the dSph by counting the number of stars in bins of 0.15 magnitudes down to the completeness limit of the survey, $i = 22$. In §5.1 we derived the structural parameters of Leo I, and these were used to define the areas from which to draw the core and field populations. The core population was taken from within an ellipse with a semi-major axis of $12'$ (approximately the tidal radius), while the field population was defined to be that beyond a semi-major axis of $30'$. Both functions were corrected for incompleteness using the estimates listed in Table 1. The Leo I LF was derived to be the difference between the core and field functions (after scaling the field function to match the area from which the core population was drawn).

Fig. 11 (top panel) shows the completeness-corrected and background-subtracted i band luminosity function of Leo I. The error-bars are the combination of Poisson uncertainties for the field and core populations, including those taken from the completeness corrections. Our magnitude limit of $i = 22$ excludes part of the red clump and the horizontal branch of Leo I. Held et al. (2000) have shown that the morphology of the Leo I horizontal branch is remarkably similar to that of the intermediate-metallicity globular cluster M5 (NGC5904; Sandquist et al. 1996). Hence, to account for the missing flux of stars fainter than our i band cutoff we supplemented the LF of Leo I with the one for M5 given in Sandquist et al. (1996). This step required a conversion of the Leo I luminosity function to the Johnson-Morgan-Cousin system via the empirical relations given in Smith et al. (2002). Distance moduli of 22.02 ± 0.13 (Leo I; Bellazzini et al. 2004) and 14.41 ± 0.07 (M5; Sandquist et al. 1996) allowed us to place the LFs on the same magnitude scale. Finally, the functions were aligned by minimizing the difference in the overlapping magnitude range. To estimate the errors of such a procedure we scaled the two LFs using the overlapping range (i) only to $I_c = 20.55$ (corresponding to $i = 21$) since our mean photometric errors beyond this limit are quite high, i.e. 0.08 ± 0.02 , and; (ii) with no upper or lower

limits.

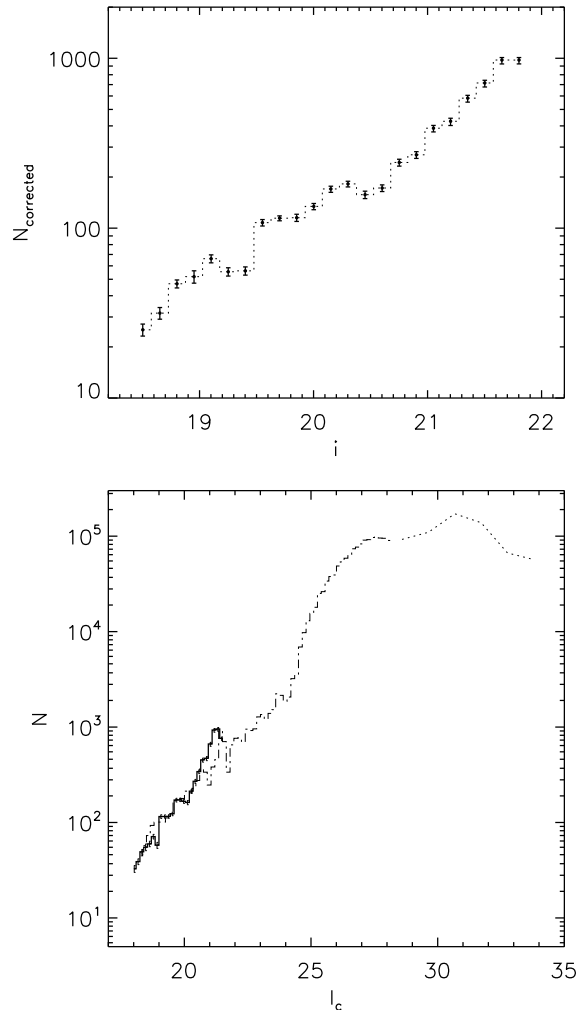


FIG. 11.— Top panel: Leo I i band luminosity function (LF) corrected for the contribution of field stars and completeness (see text for details). The indicated errors correspond to Poisson and completeness uncertainties for field and Leo I stars added in quadrature. The width of the magnitude bins is 0.15 mag. Bottom panel: Johnson-Morgan-Cousins I_c band luminosity function of Leo I (bold line) supplemented with the LF of the intermediate-metallicity globular cluster M5 (NGC5904; thin dash-dotted line) from Sandquist et al. (1996) and NGC6397 given by Piotto et al. (1997) (thin dotted line). The first LF was scaled to the distance and number counts (N) of Leo I and the latter to the extrapolated LF of Leo I (see text for details).

Furthermore, we accounted for the missing flux beyond $I_c = 27.5$ using the completeness corrected LF for NGC6397 given in Piotto et al. (1997). We chose NGC6397 since it has a metallicity comparable to the metallicity of Leo I. We used the distance modulus for NGC6397 given in Piotto et al. (1997) and scaled it to the LF of M5 which has been previously scaled to the LF of Leo I as described above. The resulting supplemented LF of Leo I is shown in the bottom panel of Fig. 11. It is in excellent agreement with the LF of Leo I presented in Lee et al. (1993) out to a magnitude of $I_c \sim 23$, beyond which their counts are dominated by incompleteness. By integrating over the luminosity function we calculated the total I_c absolute magnitude of Leo I to be

$M_{I_c} = -12.03 \pm 0.14$. Assuming a solar absolute magnitude of $M_{I_c, \odot} = 4.14$ (Odenkirchen et al. 2001) yields the total luminosity of Leo I of $L_{I_c} = (3.0 \pm 0.3) \times 10^6 L_{I_c, \odot}$.

6.2. Total mass estimate and mass-to-light ratio

We estimate the central mass-to-light ratio, and on this basis the total mass, of Leo I using the Jeans equation for an isotropic spherical stellar system (c.f. Binney & Tremaine 1987):

$$\frac{1}{\rho_*} \frac{d(\sigma_*^2 \rho_*)}{dr} = -\frac{GM(< r)}{r^2} \quad (9)$$

where r is the radius, σ_* is the stellar velocity dispersion, ρ_* is the stellar density. The right hand term in eq. [9] represents the gravitational force of the system given in terms of the total (i.e. stellar and dark matter) mass, M , within a radius r . For a simplified solution of eq. [9] we assume that the whole stellar system resides in a dark matter halo which dominates the mass.

To solve eq. [9] analytically for ρ_{DMH} we need to find a simple model that describes the stellar volume-density distribution. In §5.2 we have shown that the stellar surface-density (that is, the projected stellar volume-density) profile is well fitted by a Gaussian function (out to a radius of $\sim 12'$). Since the projection of a 3-dimensional Gaussian distribution is again a Gaussian, we adopt $\rho_*(r) = \rho_{*,0} \exp(-r^2/2r_0^2)$. We also make the ansatz that $\sigma_* \approx \text{constant}$, which leads to a solution of eq. [9] with a central mass density:

$$\rho_{\text{DM},0} = \left(\frac{3}{4\pi} \right) \frac{\sigma_*^2}{Gr_0^2} \quad (10)$$

Mateo et al. (1998b) reported a velocity dispersion for the core of Leo I of $(8.8 \pm 1.3) \text{ km s}^{-1}$ based on 33 red giants in the dSph. The average angular separation of the observed stars from the center of the galaxy was $1.9'$ with a largest separation of $3.5'$. They have also shown that there is no significant variation of the velocity dispersion with stellar type or radius. Therefore, the ansatz that σ_* is constant is a reasonable assumption, at least in the central part of Leo I. Hence, within a radius of $\sim 3.5'$ around the center of Leo I the dark matter mass density is $\rho_{\text{DM},0} = (0.07 \pm 0.02) M_{\odot} \text{ pc}^{-3}$ which corresponds to a central M/L ratio of ~ 3 in solar I_c band units. Here the reported uncertainties are formal statistical uncertainties.

The inferred central mass density is comparable to the central density of the Fornax dSph (Mateo et al. 1991) and Leo II (Vogt et al. 1995). This is consistent with the DM central densities for low-luminosity, gas-rich dwarf irregulars (for a review see Mateo et al. 1991). On the other hand, it is lower than the central densities inferred for other Local Group dSph galaxies (see e.g. Mateo et al. 1991 and Mateo 1998a for a review). Such a result may argue in favor of DM in Local Group dSphs being governed by Galactocentric distance; we discuss this in more detail in §7.

With the limited kinematic data-set in hand we can only bracket the possible M/L ratio of Leo I (within the tidal radius) by investigating two limiting cases:

(i) We assume that the total mass profile follows the light distribution. Although this assumption is not very likely

(e.g. Mateo et al. 1991; Kleyna et al. 2001), it provides a good constraint to the minimum mass of Leo I. The total mass is then given by:

$$M_{\text{tot}} = 4\pi \int_0^{\infty} \rho_{\text{mass}}(r) r^2 dr = (2\pi)^{3/2} \rho_{\text{DM},0} r_0^3 \quad (11)$$

The total mass of Leo I is then $(1.7 \pm 0.2) \times 10^7 M_{\odot}$, with quoted formal errors. Using the total luminosity of Leo I derived in the previous section we infer a mean I_c band mass-to-light ratio of ~ 6 in solar units.

(ii) We assume that the mass-density stays constant towards large radii, i.e. $\rho_{\text{mass}}(r) = \rho_{\text{DM},0}$. The total mass within a given radius is then:

$$M(r) = 4\pi \int_0^r \rho_{\text{DM},0} r'^2 dr' = \frac{4\pi}{3} \rho_{\text{DM},0} r^3 \quad (12)$$

In this case the total mass of Leo I within $r = 12'$ is $(20 \pm 6) \times 10^7 M_{\odot}$ and the mean mass-to-light ratio in the I_c band is ~ 75 in solar units.

Hence, for the two limiting descriptions of the distribution of mass in Leo I we infer an I_c band M/L ratio of 6 and 75 in solar units, respectively. If we adopt the mean $V - I_c$ color for Leo I of roughly 0.6 (see CMDs in Lee et al. 1993 and Caputo et al. 1999), then the V band M/L ratio is about 5.5 and 65 in solar units, respectively, for the two limiting cases.

7. DISCUSSION

We have estimated the mass-to-light ratio of Leo I in the I_c band to be in the range of 6 – 75 in solar units. The lower limit was calculated under the assumption that mass follows light. The upper limit represents the M/L ratio within $\sim 12'$ of a system with a large dark matter halo extending far beyond the limiting radius of the visible matter, where the dark matter halo density is constant within the luminous limiting radius. However, given the current evidence concerning dark matter halos in dwarf galaxies, it is possible to put constraints on which of these scenarios is the most likely.

If the distribution of mass follows the distribution of the visible component, then the velocity dispersion of Leo I would be expected to fall to zero at the tidal radius. Nonetheless, past studies have shown that such a behaviour is not typical for Local Group dSphs. For example, Kleyna et al. (2001) have shown that the radial variation of the velocity dispersion of the Draco dSph is flat within the uncertainties. Additional evidence for a flat velocity dispersion profile is given by Mateo et al. (1991) for the Fornax dSph. The evidence is similar for Leo I. Koch et al. (2007) report that the velocity dispersion profile of Leo I appears constant at increasing radii. This suggests that mass does not follow light in Leo I and favours option (ii). We infer that the Leo I M/L ratio is $\gg 5$ in the V band. The inferred upper value of the M/L ratio in the V band is ~ 65 , yet this represents the M/L ratio only within $\sim 12'$; hence the possibility that the true M/L ratio of Leo I is even greater than this is not ruled out.

It has been argued (for example, Klessen & Kroupa 1998) that distortion due to the Galactic tidal field can reproduce the appearance of a system dominated by dark

matter. Under this scenario, the gravitational potential of the Galaxy has heated the internal structure of an orbiting satellite, thereby leading to an inflated velocity dispersion. If we assume a *stellar* M/L of 3 for Leo I, then the velocity dispersion must be inflated by a factor of 4–5 to produce an *apparent* M/L of 65. Given that Leo I is the farthest known dSph from the Galactic center, it would be surprising to find tidal forces strong enough to alter the internal kinematics to such a degree. Indeed, our analysis found no evidence of tidal disruption. In §5.3 we demonstrated that the structure of Leo I follows a smooth, elliptical shape to the limiting radius. Thus, it seems unlikely that tidal forces are responsible for the large measured M/L value, and this result suggests that Leo I is strongly dominated by dark matter.

8. SUMMARY

We have presented an automatic photometric pipeline especially designed for SDSS crowded-field images. The software performs extremely well on crowded SDSS images, yielding high-quality photometry with completeness above 80% down to a magnitude of $\lesssim 21$ and stellar density of up to ~ 200 arcmin $^{-2}$. We have extensively tested the detection efficiency and photometric accuracy of this software (as a function of both magnitude and stellar density). The pipeline was applied to a region of $\sim 3.55^\circ$ around the dwarf spheroidal galaxy Leo I in the three bands g , $^\circ$ and i .

We constructed a filter in colour-magnitude space targeting the Leo I red giant branch. It removed $\sim 80\%$ of the foreground contamination, and enhanced the central stellar density contrast by a factor of $\gtrsim 4$. We find that the projected spatial structure of Leo I is ellipsoid-like with core and tidal radii (following an empirical King model) of $(6.21 \pm 0.95)'$ and $(11.70 \pm 0.87)'$, respectively. This corresponds to (460 ± 75) pc and (860 ± 86) pc, respectively. The radial profile deviates slightly from the King profile towards the outer regions, however there is no evidence for extra-tidal structures (such as tidal tails) down to a magnitude of $i = 22$ and at a stellar surface-density of 4×10^{-3} of the dSph's central density.

The luminosity of Leo I was measured by integrating the observed completeness-corrected and background-subtracted flux of stars. We accounted for the missing flux to the faintest levels ($I_c=34$) supplementing the luminosity function with the LFs of the globular clusters M5 and NGC6397. The I_c band absolute magnitude of Leo I was measured to be $M_{I_c} = -12.03 \pm 0.14$ and the total luminosity $(3.0 \pm 0.3) \times 10^6 L_{I_c, \odot}$.

We modelled the mass of Leo I using the spherical Jeans equation and assumed that the stellar velocity dispersion is isotropic and spatially constant. The inferred central mass density of Leo I is then $(0.07 \pm 0.02) M_\odot \text{pc}^{-3}$. Assuming that mass follows light the total mass of Leo I is $(1.7 \pm 0.2) \times 10^7 M_\odot$. This value is comparable to the total mass estimates using the standard 'core' fitting method. Under the assumption that the dark matter halo is extended and its density is spatially constant, the total mass of Leo I within the tidal radius of the visible component (i.e. $12'$) is $(2 \pm 0.6) \times 10^8 M_\odot$. Hence, the total mass to light ratio for Leo I in the I_c band and in solar units is in the range of about 6 to 75, where the first and latter values correspond to the above quoted masses, respectively. In Sec. 7 we argued that the mass-follows-light assumption is not reasonable for the Leo I system and therefore concluded that the M/L ratio must be $\gg 6$ in I_c band solar units and possibly > 75 if a constant density DM halo would dominate the mass and extend further beyond $12'$.

The authors would like to thank the referee M. Irwin for constructive suggestions which helped to improve the paper. VS thanks MM, DR and BB for sincere and enormous support during the creation of this paper; Frank van den Bosch and Robert Lupton for insightful discussions; and Andreas Koch and collaborators for sharing their results with us prior to publication.

Funding for the Sloan Digital Sky Survey (SDSS) has been provided by the Alfred P. Sloan Foundation, the Participating Institutions, the National Aeronautics and Space Administration, the National Science Foundation, the U.S. Department of Energy, the Japanese Monbukagakusho, and the Max Planck Society. The SDSS Web site is <http://www.sdss.org/>.

The SDSS is managed by the Astrophysical Research Consortium (ARC) for the Participating Institutions. The Participating Institutions are The University of Chicago, Fermilab, the Institute for Advanced Study, the Japan Participation Group, The Johns Hopkins University, the Korean Scientist Group, Los Alamos National Laboratory, the Max-Planck-Institute for Astronomy (MPIA), the Max-Planck-Institute for Astrophysics (MPA), New Mexico State University, University of Pittsburgh, University of Portsmouth, Princeton University, the United States Naval Observatory, and the University of Washington.

REFERENCES

- Abazajian, K., et al. 2003, AJ, 126, 2081
 Abazajian, K., et al. 2004, AJ, 128, 502
 Abazajian, K., et al. 2005, AJ, 129, 1755
 Adelman-McCarthy, J. K., et al. 2006, ApJS, 162, 38
 Adelman-McCarthy, J. K., et al. 2007, ApJS, in press
 Bellazzini, M., Gennari, N., Ferraro, F. R., & Sollima, A. 2004, MNRAS, 354, 708
 Belokurov, V., Evans, N. W., Irwin, M. J., Hewett, P. C., & Wilkinson, M. I. 2006, ApJ, 637, L29, 2006a
 Belokurov, V., et al. 2006b, ApJ, 642, L137, 2006b
 Belokurov, V., et al. 2006c, ArXiv Astrophysics e-prints, arXiv:astro-ph/0604355
 Belokurov, V., et al. 2006d, ArXiv Astrophysics e-prints, arXiv:astro-ph/0605705
 Bowen, D. V., Tolstoy, E., Ferrara, A., Blades, J. C., & Brinks, E. 1997, ApJ, 478, 530
 Byrd, G., Valtonen, M., McCall, M., & Innanen, K. 1994, AJ, 107, 2055
 Caputo, F., Cassisi, S., Castellani, M., Marconi, G., & Santolamazza, P. 1999, AJ, 117, 2199
 Demers, S., Irwin, M. J., & Gambu, I. 1994, MNRAS, 266, 7
 Dressel, L. L., & Condon, J. J. 1976, ApJS, 31, 187
 Fox, M. F., & Pritchett, C. J. 1987, AJ, 93, 1381
 Falco, E. E., et al. 1999, PASP, 111, 438
 Fukugita, M., Ichikawa, T., Gunn, J. E., Doi, M., Shimasaku, K., & Schneider, D. P. 1996, AJ, 111, 1748
 Gallart, C., Freedman, W. L., Aparicio, A., Bertelli, G., & Chiosi, C. 1999a, AJ, 118, 2245, 1999a
 Gallart, C., et al. 1999, ApJ, 514, 665, 1999b

- Gallouët, L., & Heidmann, N. 1971, *A&AS*, 3, 325
- Grillmair, C. J., Freeman, K. C., Irwin, M., & Quinn, P. J. 1995, *AJ*, 109, 2553
- Grillmair, C. J., & Dionatos, O. 2006, *ApJ*, 643, L17
- Harrington, R. G., & Wilson, A. G. 1950, *PASP*, 62, 118
- Held, E. V., Saviane, I., Momany, Y., & Carraro, G. 2000, *ApJ*, 530, L85
- Held, E. V., Clementini, G., Rizzi, L., Momany, Y., Saviane, I., & Di Fabrizio, L. 2001, *ApJ*, 562, L39
- Helmi, A., et al. 2003, *ApJ*, 586, 195, 2003a
- Helmi, A., Navarro, J. F., Meza, A., Steinmetz, M., & Eke, V. R. 2003b, *ApJ*, 592, L25, 2003b
- Irwin, M., & Hatzidimitriou, D. 1995, *MNRAS*, 277, 1354; IH95
- Juritsch, M., et al. 2005, *ArXiv Astrophysics e-prints*, arXiv:astro-ph/0510520
- Klessen, R. S., & Kroupa, P. 1998, *ApJ*, 498, 143
- Kleyna, J. T., Wilkinson, M. I., Evans, N. W., & Gilmore, G. 2001, *ApJ*, 563, L115
- Koch, A., Wilkinson, M. I., Kleyna, J. T., Gilmore, G. F., Grebel, E. K., Mackey, A. D., Evans, N. W., & Wyse, R. F. G. 2007, *ApJ*, 657, 241
- Lee, M. G., Freedman, W., Mateo, M., Thompson, I., Roth, M., & Ruiz, M.-T. 1993, *AJ*, 106, 1420
- Lupton, R. H., Ivezić, Z., Gunn, J. E., Knapp, G., Strauss, M. A., & Yasuda, N. 2002, *Proc. SPIE*, 4836, 350
- Lynden-Bell, D. 1999, *IAU Symposium*, 192, 39
- Martínez-Delgado, D., Alonso-García, J., Aparicio, A., & Gómez-Flechoso, M. A. 2001, *ApJ*, 549, L63
- Mateo, M., Olszewski, E., Welch, D. L., Fischer, P., & Kunkel, W. 1991, *AJ*, 102, 914
- Mateo, M. L. 1998, *ARA&A*, 36, 435; 1998a
- Mateo, M., Olszewski, E. W., Vogt, S. S., & Keane, M. J. 1998, *AJ*, 116, 2315; 1998b
- Odenkirchen, M., et al. 2001, *AJ*, 122, 2538
- Oke, J. B., & Gunn, J. E. 1983, *ApJ*, 266, 713
- Palma, C., Majewski, S. R., Siegel, M. H., Patterson, R. J., Ostheimer, J. C., & Link, R. 2003, *AJ*, 125, 1352
- Peebles, P. J. E. 1995, *ApJ*, 449, 52
- Pier, J. R., Munn, J. A., Hindsley, R. B., Hennessy, G. S., Kent, S. M., Lupton, R. H., & Ivezić, Z. 2003, *AJ*, 125, 1559
- Piotto, G., Cool, A. M., & King, I. R. 1997, *AJ*, 113, 1345
- Plummer, H. C. 1911, *MNRAS*, 71, 460
- Reid, N., & Mould, J. 1991, *AJ*, 101, 1299
- Sandquist, E. L., Bolte, M., Stetson, P. B., & Hesser, J. E. 1996, *ApJ*, 470, 910
- Schechter, P. L., Mateo, M., & Saha, A. 1993, *PASP*, 105, 1342
- Schlegel, D. J., Finkbeiner, D. P., & Davis, M. 1998, *ApJ*, 500, 525
- Smith, J. A., et al. 2002, *AJ*, 123, 2121
- Stoughton, C., et al. 2002, *AJ*, 123, 485
- Vogt, S. S., Mateo, M., Olszewski, E. W., & Keane, M. J. 1995, *AJ*, 109, 151
- Wallerstein, G., & Cox, A. N. 1984, *PASP*, 96, 677
- Willman, B., et al. 2005, *ApJ*, 626, L85
- Xu, Y., Deng, L. C., & Hu, J. Y. 2006, *MNRAS*, 368, 1811
- Yanny, B., et al. 2003, *ApJ*, 588, 824
- York, D. G., et al. 2000, *AJ*, 120, 1579
- Zaritsky, D., Olszewski, E. W., Schommer, R. A., Peterson, R. C., & Aaronson, M. 1989, *ApJ*, 345, 759
- Zaritsky, D. 1999, *ASP Conf. Ser.* 165: The Third Stromlo Symposium: The Galactic Halo, 165, 34
- Zucker, D. B., et al. 2006, *ApJ*, 643, L103
- Zwicky, F., Herzog, E., & Wild, P. 1961, *CGCG1*, 0